Electrical Readout of Individual Nuclear Spin Trajectories in a Single-Molecule Magnet Spin Transistor

S. Thiele,[1] R. Vincent,[1] M. Holzmann,[2] S. Klyatskaya,[3] M. Ruben,[3,4] F. Balestro,[1] and W. Wernsdorfer[1]

[1]*Institut Néel, CNRS and Université Joseph Fourier, B.P. 166, 38042 Grenoble Cedex 09, France*
[2]*LPMMC, Maison des Magistères, Grenoble, and LPTMC, Jussieu, Paris, France*
[3]*Institute of Nanotechnology, Karlsruhe Institute of Technology, 76344 Eggenstein-Leopoldshafen, Germany*
[4]*Institut de Physique et Chimie des Materiaux de Strasbourg, CNRS, 67034 Strasbourg, France*

We present the electrical readout of time trajectories obtained from an isolated nuclear spin. The device, a $TbPc_2$ single-molecule magnet spin transistor, detects the four different nuclear spin states of the Tb^{3+} ion with fidelities better than 69%, allowing us to measure individual relaxation times (T_1) of several tens of seconds. A good agreement with quantum Monte Carlo simulations suggests that the relaxation times are limited by the current tunneling through the transistor, which opens up the possibility to tune T_1 electrically by means of bias and gate voltages.

The key problems in spin-based quantum electronic devices are the long-term information storage on single spins and the nondestructive retrieval of the latter. Moreover, the ability to perform all operations electrically is advantageous to interconnect classical and quantum electronics. A promising approach involves the use of electron spins confined in quantum dots [1–5]. However, storage of quantum information is severely limited due to short spin lifetimes. To overcome this problem, it was suggested to use nuclear spins instead [6]. Its excellent intrinsic isolation from the environment leads to very long relaxation (T_1) and coherence (T_2) times. However, this property also brings a significant disadvantage because it considerably impedes addressing and reading single nuclear spins with high fidelity.

Up to now, the most advanced experiments with the ability to read out and manipulate single nuclear spins are performed using nitrogen-vacancy centers [7–10]. However, a coupling to classical electronics requires additional optical transducers. More recently, a complete electronic readout of a single nuclear spin was performed on single-molecule magnet (SMM) based devices [11–13] and silicon based devices [14]. One of the main advantages of using SMMs as building blocks is the possibility to chemically tailor their properties to meet almost any required needs, such as magnetic anisotropy or chemical affinity for self-assembly device fabrication. Additionally, they are highly versatile and can be integrated into any conceivable nanoscale device [15,16]. Moreover, preliminary experiments on assemblies of SMMs revealed a multitude of quantum phenomena such as quantum tunneling of magnetization (QTM) [17,18], quantum phase interference [19], and coherence [20].

Here, we present the electrical readout of an isolated nuclear-spin trajectory allowing for the extraction of the state-dependent relaxation times. By comparing the results

with constitutive quantum Monte Carlo (QMC) simulations, we were able to establish the dominating relaxation process. Based on these results, the electrical manipulation of the nuclear spin lifetime was demonstrated.

All experimental results were obtained via electric transport measurements through a three-terminal single-molecule spin transistor [Fig. 1(a)] placed into a dilution refrigerator at 150 mK. The transistor was fabricated using electromigration at low temperature [21]. In this way, a nanometer sized gap was crafted between two very clean gold terminals, in which we trapped a bis(phthalocyaninato) terbium (III) SMM ($TbPc_2$). The heart of the molecule is a Tb^{3+} ion, which is sandwiched between two organic phthalocyanine (Pc) ligands [Fig. 1(a)]. The Tb^{3+} ion has an electronic configuration of $[Xe]4f^8$ resulting in a total spin of $S = 3$ and a total orbital momentum of $L = 3$. A strong spin-orbit coupling yields an electronic spin with a total angular magnetic moment of $J = 6$ [22]. In addition, the ligand field, generated by the two Pc's, leads to a well isolated electron-spin ground state doublet of $m_J = \pm 6$ with a uniaxial anisotropy axis perpendicular to the Pc plane [23]. The off diagonal terms in the ligand-field Hamiltonian are slightly mixing the spin states. In addition to the electronic spin, the Tb^{3+} ion has a nuclear spin of $I = 3/2$. A very large hyperfine interaction results in a fourfold level splitting of each electronic spin state. The ground state doublet has, therefore, four avoided energy level crossings [shaded rectangles in Fig. 1(b)].

At low temperatures, the Tb electronic spin can reverse in two different ways. It can relax via a direct relaxation process from the excited to the ground state involving the creation of a phonon to account for the energy and momentum conservation. This process is proportional to B^3 and dominates only at higher magnetic fields (hundreds of mT). The second possibility is a QTM transition, which dominates at small magnetic fields and can happen at
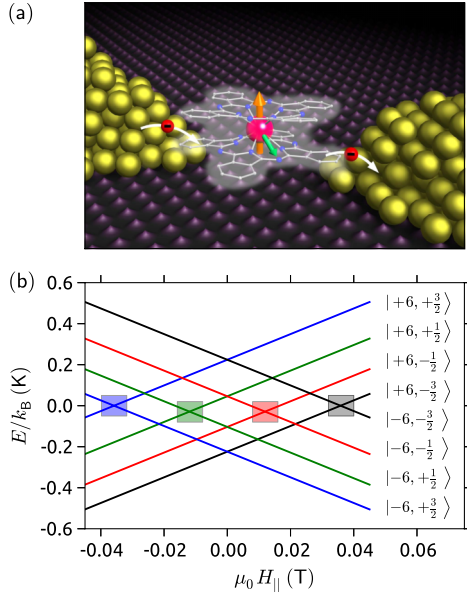
(a)

(b)

FIG. 1 (color online). (a) Artist view of the molecular spin transistor, consisting of a TbPc$_2$ molecular magnet, connected to source and drain gold electrodes, and a back gate underneath. The Pc ligands (white cloud) are acting as a readout quantum dot. The terbium ion (pink sphere in the center) possesses an electronic spin with $J = 6$ (orange upward arrow) and a nuclear spin with $I = 3/2$ (green sideward arrow). The uniaxial anisotropy axis of the Tb ion is perpendicular to the Pc plane. (b) Zeeman diagram of the energy levels of the TbPc$_2$ molecule with the magnetic field parallel to the easy axis of magnetization ($H_\parallel$). Because of a strong hyperfine interaction with the Tb nuclear spin, the electron's up and down states are each split into four energy levels. Off diagonal terms in the spin Hamiltonian lead to avoided energy level crossings (shaded rectangles), enabling tunneling of the electronic spin. Note that for each QTM transition, the nuclear spin is preserved and therefore, their positions reveal the nuclear spin states.

avoided energy level crossings. When the magnetic field is swept over such an avoided crossing, there is a certain probability P_{LZ} to tunnel from one state into the other. The magnitude of P_{LZ} can be calculated by the Landau-Zener (LZ) formula [24]. As shown in Fig. 1(b), there are four of those avoided-level crossings and therefore, four different regions in magnetic field for QTM transitions among which the nuclear spin is always preserved. Hence, the four transitions can be used to identify the four nuclear spin states.

In order to reliably detect the electronic spin reversal, we used a quantum dot or readout dot, which was ferromagnetically coupled to the Tb electronic spin [11]. The coupling was determined by studying the influence of the Tb electronic spin on the spin 1/2 Kondo ridge of the readout dot [11]. The magnitude of the interaction indicated that the readout dot was created by the two Pc ligands with their delocalized π-electron systems [white cloud in Fig. 1(a)]. The working point of the readout dot was adjusted with the gate voltage and was found to be best in between Coulomb

blockade and maximum transparency. Whenever the Tb electronic spin reversed, the chemical potential of the readout dot changed and thus, gave rise to a sharp conductance jump [11] (for further explanation, see Supplemental Material [25]).

We aligned the external magnetic field using a homemade 3D vector magnet with the easy axis of the TbPc$_2$ and constantly ramped it up and down between ± 60 mT [Fig. 2(a)]. By simultaneously monitoring the conductance of the readout dot, we observe conductance jumps happening at four distinct magnetic fields, which can account for QTM transitions of the Tb electronic spin [Fig. 2(b)]. From the four unique positions of the jumps, we yielded the four nuclear spin states and thus, were able to reconstruct the nuclear spin trajectory. For statistical analysis, this procedure was repeated 80 000 times. The first 500 seconds of the nuclear spin trajectory are shown in Fig. 3(a). Note that due to the probabilistic nature of the tunnel mechanism, we observed QTM transitions in $\approx 51\%$ of all sweeps (see Supplemental Material [25]). By plotting all detected jumps in histograms [Fig. 3(b)], we obtain four nonoverlapping Gaussian-like distributions where $(95 \pm 2)\%$ of all measured events are found within the shaded rectangles. The widths of the histograms was dominated by electronic noise and the finite response time of the lock-in amplifier used to measure the conductance jumps.

The time-average population of each state was obtained through integration of the Gaussian-like distributions [shaded bars, Fig. 3(b)]. By further analyzing the data shown in Fig. 3, we extracted the different dwell times for each nuclear-spin state. Plotting those data in renormalized histograms yielded the time dependence of each
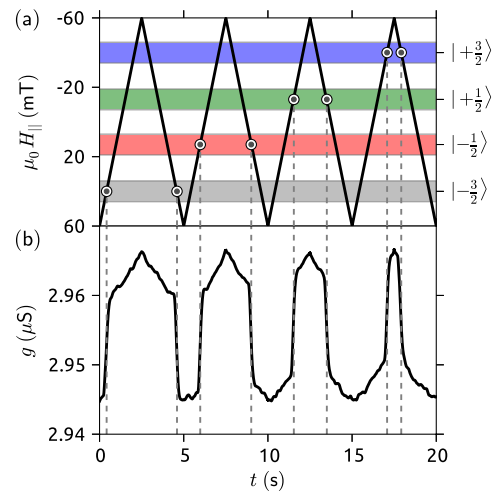
(a)

(b)

FIG. 2 (color online). Scheme of the measurement procedure. (a) The magnetic field $H_\parallel$ is swept up and down as a function of time t over the four avoided level crossings and (b) the conductance g through the readout dot is simultaneously measured. Whenever the electronic spin undergoes a QTM transition, a conductance jump is observed (indicated by dashed lines) revealing the nuclear spin state.
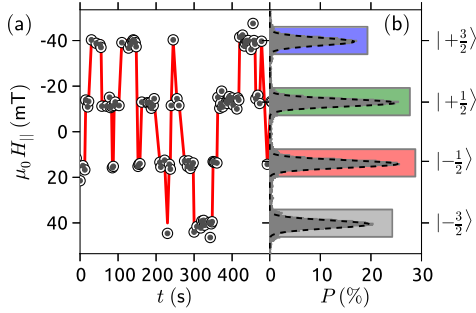
FIG. 3 (color online). Nuclear spin trajectory. (a) By continuously ramping the magnetic field up and down, the conductance jumps reveal the nuclear spin states (gray dots) as a function of time, yielding the nuclear spin trajectory (red curve). We found that the nuclear spin quantum number changes only by $\Delta m_I = \pm 1$ (see Supplemental Material [25]). (b) Histograms (gray) of about 40 000 conductance jumps, showing four nonoverlapping Gaussian-like distributions (dashed lines). The shaded bars, obtained by counting all events lying within three times the full width half maximum of the fitted Gaussians, contain $(95 \pm 2)\%$ of the data points and represent the time-average population P of each nuclear spin state.

nuclear-spin expectation value [Figs. 4(a)–4(d)]. A further fitting to exponentials gave the individual relaxation times T_1. The perfect exponential decay indicated that no memory effect is present in the system. Furthermore, the obtained lifetimes were an order of magnitude larger than the
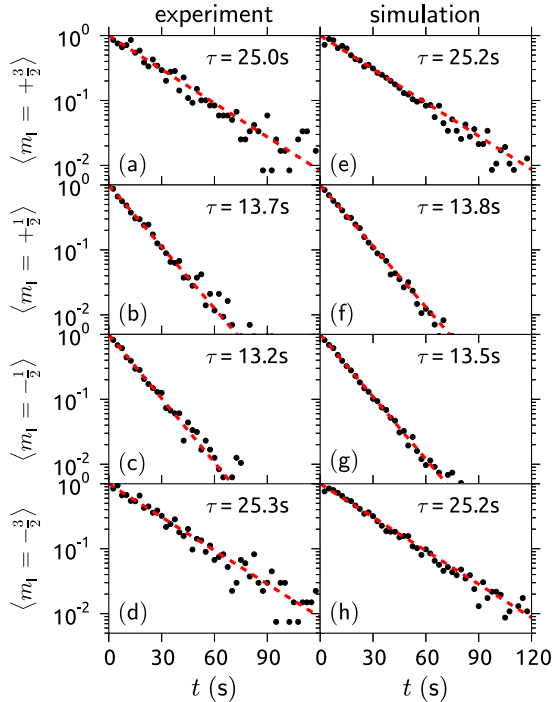

FIG. 4 (color online). (a)–(d) Measured expectation value and (e)–(h) QMC simulations of each nuclear spin state versus time. The given T_1 values were obtained by fitting the data to an exponential function $\exp(-t/T_1)$ (red dashed lines).

measurement interval, which is a proof of the quantum nondemolition nature of the detection scheme. The readout fidelities F are obtained by calculating the probability to stay in the state during the time necessary to measure it. Because of the QTM probability of 51%, two subsequent measurements are separated by 5 s in average resulting in fidelities of $F(m_I = \pm 3/2) \approx \exp(-5\,\text{s}/25.2\,\text{s}) \approx 82\%$ and $F(m_I = \pm 1/2) \approx \exp(-5\,\text{s}/13.2\,\text{s}) \approx 69\%$.

In contrast to [11], the average time between two subsequent measurements is smaller than T_1. Since each measurement is inverting the nuclear energy levels, the system is driven out of thermal equilibrium. In order to get a deeper understanding of the nuclear spin trajectory obtained under such nonequilibrium conditions, we performed quantum Monte Carlo (QMC) simulations using the QMC wave function approach [26–28] (see Supplemental Material [25]). The nuclear spin was modeled as a four-level system ($2I + 1$ states) which was coupled to a thermal bath of temperature $T = 150$ mK (cryostat temperature). The Hamiltonian of the isolated nuclear spin H_0 is mainly determined by its quadrupole moment, resulting in unequal nuclear level spacings of $\omega_{0,1} = 121$ mK, $\omega_{1,2} = 149$ mK, and $\omega_{2,3} = 178$ mK [23]. All environmental contributions were combined in an effective Hamiltonian with non-Hermitian perturbation H_1:

$$H_1 = -\frac{i\hbar}{2}\sum_m C_m^\dagger C_m, \tag{1}$$

where m represents all possible transition paths. We further assumed that transitions between those three levels are only allowed if $\Delta m_I = \pm 1$, leading to one relaxation and one excitation path for each transition (i, j), modeled by $C_1^{i,j}$ and $C_2^{i,j}$, respectively:

$$C_1^{i,j} = \sqrt{\Gamma_{i,j}[1 + n(\omega_{i,j}, T)]}\,\delta_{i,j+1}, \tag{2}$$

$$C_2^{i,j} = \sqrt{\Gamma_{i,j}[n(\omega_{i,j}, T)]}\,\delta_{i+1,j}, \tag{3}$$

where $n(\omega_{i,j}, T) = [\exp(\hbar\omega_{i,j}/k_B T) - 1]^{-1}$ is the Bose-Einstein distribution function and $\Gamma_{i,j}$ is the transition rate between the ith and the jth nuclear spin state. Note that the three $\Gamma_{i,j}$'s were the only adjustable parameters in the simulation. The transition probability dp for each level and time step dt is then calculated as:

$$dp = \langle \Psi(t)|C_1^\dagger C_1 + C_2^\dagger C_2|\Psi(t)\rangle dt. \tag{4}$$

The nonequilibrium dynamics is introduced by sweeping the magnetic field in intervals of $\Delta t = 2.5$ s back and forth. Every time we reached one of the four avoided level crossings, we swapped the ground state and the excited states with the experimentally obtained QTM probability. Since $\Delta t < T_1$, we get a nonequilibrium distribution. To compute a nuclear spin trajectory of several days, we repeated this procedure 2^{24} times.
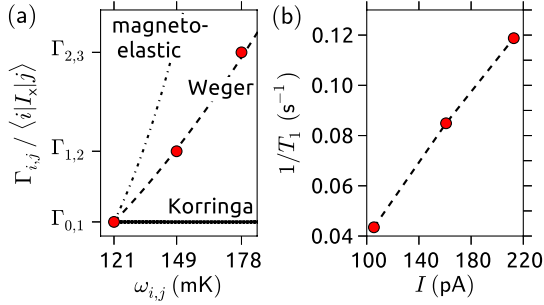
FIG. 5 (color online). (a) The transition rates $\Gamma_{i,j}$, derived by fitting the results of QMC simulations to experimental data, exhibit a quadratic dependence on the nuclear spin level spacing $\omega_{i,j}$. This behavior is expected from a Weger relaxation process in which the nuclear spin is coupled via virtual spin waves to conduction electrons. (b) The decrease of lifetime with increasing current is probably due to an increase of electrons tunneling through the readout dot in addition to an increase of temperature.

From the simulated data, we extracted the relaxation times T_1 of each nuclear spin state [Figs. 4(e)–4(h)] and obtained a perfect agreement with our experiment. The difference in lifetime between the $\pm 3/2$ and $\pm 1/2$ states comes from the fact that the nuclear spin in the $\pm 3/2$ states has only one escape path (excitation *or* relaxation), whereas the nuclear spin in the $\pm 1/2$ has two escape paths (excitation *and* relaxation). Since the lifetime is roughly inversely proportional to the number of transition paths, the T_1's show a difference of approximately two. The exact ratio depends of course on temperature and the individual transition rates.

In order to reveal the dominant relaxation mechanism, we considered spin-lattice interactions and nuclear spin diffusion. The latter mechanism was found to be very weak in Tb crystals [29] and can, hence, be neglected for rather isolated and nonaligned SMMs. Concerning the spin-lattice relaxation mechanism, we examined closer the $\Gamma_{i,j}$'s derived by fitting the results of QMC simulations to experimental data. Depending on its proportionality to the nuclear level spacing $\omega_{i,j}$, we can distinguish between three types of mechanisms. (i) The Korringa process in which conduction electrons polarize the inner lying s electrons. Since these couple with the nuclear spins via contact interaction, an energy exchange over this interaction chain is established, leading to $\Gamma_{i,j} \propto |\langle i|I_x|j\rangle|^2$ [30]. (ii) The Weger process, which suggests that the spin-lattice relaxation is dominated by the intraionic hyperfine interaction and the conduction electron exchange interaction [31]. It is a two-stage process, where the energy of the nucleus is transmitted to the conduction electrons via the creation and annihilation of a virtual spin wave. This process is similar to the Korringa process but results in $\Gamma_{i,j} \propto |\langle i|I_x|j\rangle|^2 \omega_{i,j}^2$. (iii) The magnetoelastic process, which leads to a deformation of the molecule due to a nuclear spin relaxation, yields $\rightarrow \Gamma_{i,j} \propto |\langle i|I_x|j\rangle|^2 \omega_{i,j}^4$ [32]. The term $|\langle i|I_x|j\rangle|^2$ arises from the fact that only rotations

of the spin perpendicular to the z directions are responsible for longitudinal transitions [33]. A comparison between the $\Gamma_{i,j}$'s and the different mechanisms is shown in [Fig. 5(a)]. The almost perfect agreement with the Weger process suggests that the dominant relaxation process is caused by the conduction electrons. Since they are ferromagnetically coupled to the Tb electronic spin, which in turn is hyperfine coupled to the nuclear spin, an energy and momentum exchange via virtual spin waves could be possible. This suggests that by controlling the amount of available conduction electrons per unit time the relaxation rate and thus, T_1 can be changed. Hence, an electrical control by means of the bias and gate voltages is possible. We performed such experiments and were able to significantly reduce the T_1 of the nuclear spin [Fig. 5(b)].

In conclusion, we demonstrated the quantum nondestructive nature of the nuclear spin detection scheme in combination with readout fidelities better than 69%. We were able to measure individual relaxation times T_1 of a single nuclear spin. In addition, quantum Monte Carlo simulations could quantitatively explain all measured features and revealed the dominant relaxation mechanism. Based on these results, we could show that T_1 can be tuned by changing the amplitude of the current tunneling through the readout dot. For example, this could be interesting to speed up the initialization of the nuclear spin in its ground state prior to a quantum operation.

[1] D. Loss and D. P. DiVincenzo, Phys. Rev. A **57**, 120 (1998).
[2] A. Imamoğlu, D. D. Awschalom, G. Burkard, D. P. DiVincenzo, D. Loss, M. Sherwin, and A. Small, Phys. Rev. Lett. **83**, 4204 (1999).
[3] J. M. Elzerman, R. Hanson, L. H. Willems van Beveren, B. Witkamp, L. M. K. Vandersypen, and L. P. Kouwenhoven, Nature (London) **430**, 431 (2004).
[4] J. A. H. Stotz, R. Hey, P. V. Santos, and K. H. Ploog, Nat. Mater. **4**, 585 (2005).
[5] F. H. L. Koppens, C. Buizert, K. J. Tielrooij, I. T. Vink, K. C. Nowack, T. Meunier, L. P. Kouwenhoven, and L. M. K. Vandersypen, Nature (London) **442**, 766 (2006).
[6] B. E. Kane, Nature (London) **393**, 133 (1998).
[7] M. V. Gurudev Dutt, L. Childress, L. Jiang, E. Togan, J. Maze, F. Jelezko, A. S. Zibrov, P. R. Hemmer, and M. D. Lukin, Science **316**, 1312 (2007).
[8] P. Neumann, J. Beck, M. Steiner, F. Rempp, H. Fedder, P. R. Hemmer, J. Wrachtrup, and F. Jelezko, Science **329**, 542 (2010).

[9] L. Robledo, L. Childress, H. Bernien, B. Hensen, P. F. A. Alkemade, and R. Hanson, Nature (London) **477**, 574 (2011).

[10] A. Dréau, P. Spinicelli, J. R. Maze, J.-F. Roch, and V. Jacques, Phys. Rev. Lett. **110**, 060502 (2013).

[11] R. Vincent, S. Klyatskaya, M. Ruben, W. Wernsdorfer, and F. Balestro, Nature (London) **488**, 357 (2012).

[12] M. Ganzhorn, S. Klyatskaya, M. Ruben, and W. Wernsdorfer, Nat. Nanotechnol. **8**, 165 (2013).

[13] M. Urdampilleta, S. Klyatskaya, M. Ruben, and W. Wernsdorfer, Phys. Rev. B **87**, 195412 (2013).

[14] J. J. Pla, K. Y. Tan, J. P. Dehollain, W. H. Lim, J. J. L. Morton, F. A. Zwanenburg, D. N. Jamieson, A. S. Dzurak, and A. Morello, Nature (London) **496**, 334 (2013).

[15] L. Bogani and W. Wernsdorfer, Nat. Mater. **7**, 179 (2008).

[16] M. Urdampilleta, S. Klyatskaya, J.-P. Cleuziou, M. Ruben, and W. Wernsdorfer, Nat. Mater. **10**, 502 (2011).

[17] J. R. Friedman, M. P. Sarachik, J. Tejada, and R. Ziolo, Phys. Rev. Lett. **76**, 3830 (1996).

[18] L. Thomas, F. Lionti, R. Ballou, D. Gatteschi, R. Sessoli, and B. Barbara, Nature (London) **383**, 145 (1996).

[19] W. Wernsdorfer and R. Sessoli, Science **284**, 133 (1999).

[20] S. Takahashi, J. van Tol, C. C. Beedle, D. N. Hendrickson, L.-C. Brunel, and M. S. Sherwin, Phys. Rev. Lett. **102**, 087603 (2009).

[21] H. Park, A. K. L. Lim, A. P. Alivisatos, J. Park, and P. L. McEuen, Appl. Phys. Lett. **75**, 301 (1999).

[22] G. S. Ofelt, J. Chem. Phys. **38**, 2171 (1963).

[23] N. Ishikawa, M. Sugita, and W. Wernsdorfer, Angew. Chem., Int. Ed. **44**, 2931 (2005).

[24] W. Wernsdorfer, R. Sessoli, A. Caneschi, D. Gatteschi, A. Cornia, and D. Mailly, J. Appl. Phys. **87**, 5481 (2000).

[25] See Supplemental Material at http://link.aps.org/supplemental/10.1103/PhysRevLett.111.037203 for details about the device fabrication and methods, the terbium double-decker complex, the nuclear spin readout, the quantum tunneling of magnetization, the quantum Monte Carlo algorithm, the dynamical equilibrium, and the selection rules.

[26] J. Dalibard, Y. Castin, and K. Molmer, Phys. Rev. Lett. **68**, 580 (1992).

[27] K. Molmer, Y. Castin, and J. Dalibard, J. Opt. Soc. Am. B **10**, 524 (1993).

[28] K. Molmer and Y. Castin, Quantum Semiclass. Opt. **8**, 49 (1996).

[29] N. Sano and J. Itoh, J. Phys. Soc. Jpn. **32**, 95 (1972).

[30] J. Korringa, Physica (Utrecht) **16**, 601 (1950).

[31] M. Weger, Phys. Rev. **128**, 1505 (1962).

[32] N. Sano, S.-I. Kobayashi, and J. Itoh, Prog. Theor. Phys. Suppl. **46**, 84 (1970).

[33] M. A. H. McCausland and I. S. Mackenzie, Adv. Phys. **28**, 305 (1979).